

Constraining Accreted Neutron Star Crust Shallow Heating with the Inferred Depth of Carbon Ignition in X-ray Superbursts

Zach Meisel^{*}

Institute of Nuclear & Particle Physics Department of Physics & Astronomy Ohio University, Athens, Ohio 45701, USA

Accepted XXX. Received YYY; in original form ZZZ

ABSTRACT

Evidence has accumulated for an as-yet unaccounted for source of heat located at shallow depths within the accreted neutron star crust. However, the nature of this heat source is unknown. I demonstrate that the inferred depth of carbon ignition in X-ray superbursts can be used as an additional constraint for the magnitude and depth of shallow heating. The inferred shallow heating properties are relatively insensitive to the assumed crust composition and carbon fusion reaction rate. For low accretion rates, the results are weakly dependent on the duration of the accretion outburst, so long as accretion has ensued for enough time to replace the ocean down to the superburst ignition depth. For accretion rates at the Eddington rate, results show a stronger dependence on the outburst duration. Consistent with earlier work, it is shown that urca cooling does not impact the calculated superburst ignition depth unless there is some proximity in depth between the heating and cooling sources.

Key words: keyword1 – keyword2 – keyword3

1 INTRODUCTION

Accreting neutron stars are unique probes of matter at high density and relatively low temperature, as well as extreme neutron-proton asymmetries (Fukushima & Hatsuda 2011; Meisel et al. 2018). A number of observables provide unique insight into the nature of these ultradense objects, including X-ray bursts, X-ray superbursts, and crust cooling after accretion outbursts (Wijnands et al. 2017; in’t Zand 2017; Galloway & Keek 2021). Model-observation comparisons are beginning to provide a handle on bulk properties of the underlying neutron star, such as the mass and radius, as well as evidence for exotic processes and phases of matter deep in the neutron star crust and even into the core (e.g Brown & Cumming 2009; Page & Reddy 2013; Deibel et al. 2017; Cumming et al. 2017; Brown et al. 2018; Meisel et al. 2019; Goodwin et al. 2019). While there have been several successes in modeling the aforementioned observed phenomena for various accreting neutron star sources, many require the addition of a heat source in the neutron star outer layers. Shallow heating has been used to explain the characteristic break in the crust cooling light curve (Degenaar et al. 2014; Turlione et al. 2015; Merritt et al. 2016; Parikh et al. 2017; Page et al. 2022), the existence of short-waiting time bursts in X-ray bursting systems (Keek & Heger 2017), and is likely necessary to resolve the discrepancy between modeled and inferred superburst ignition depths (Cooper et al. 2009).

The physical mechanism for the shallow heat source is not known, which is one of the major outstanding problems in accreting neutron star physics (Schatz et al. 2022a). Nuclear reactions are known to be an important crustal heat source (Gupta et al. 2007; Gupta et al. 2008; Steiner 2012); however, both the depth and magnitude of this heat appear to be inconsistent with observational constraints for shallow

heating (Brown & Cumming 2009; Deibel et al. 2015; Fantina et al. 2018; Chamel et al. 2020). Other suggested heat sources are related to compositionally driven convection in the accreted neutron star ocean and transfer of energy from the accretion flow to deeper depths via gravity waves (Inogamov & Sunyaev 2010; Medin & Cumming 2015; Deibel et al. 2015). Determining if any of these explanations, or some combination thereof, ultimately suffice will require concerted model-observation comparison efforts.

Crust cooling model-observation comparisons likely provide the most stringent constraints on shallow heating, as the quiescent cooling light curve provides a tomographic picture of the accreted crust (Page & Reddy 2013). However, these model calculations have a large number of poorly-constrained parameters and therefore many degenerate solutions as to the strength and depth of shallow heating. As such, complementary constraints on the properties of shallow heating in accreting neutron star crusts are desirable. The inferred depth of carbon ignition for X-ray superbursts provides such an opportunity.

X-ray superbursts are thought to be energetic explosions ignited by carbon fusion in the accreted neutron star ocean and primarily powered by the photodisintegration of heavy nuclei remaining from earlier surface burning (Taam & Picklum 1978; Cumming & Bildsten 2001; Strohmayer & Brown 2002; Cornelisse et al. 2003; Schatz et al. 2003). The ignition column depth can be roughly inferred based on the typical recurrence time $\Delta t_{\text{rec}} \sim 1$ yr and accretion rate $\dot{M} \sim 5 \times 10^{-9} M_{\odot}/\text{yr}$ for superbursting systems (in’t Zand et al. 2003; Galloway et al. 2020) as $y_{\text{ign}} = \dot{M} \Delta t_{\text{rec}} / (4\pi R_{\text{NS}}^2) \sim 5 \times 10^{11} \text{ g cm}^{-2}$ (Meisel et al. 2018), assuming a neutron star radius $R_{\text{NS}} \sim 12$ km (Riley et al. 2021). A more rigorous analysis based on fitting the observed superburst light curve with cooling models results in the ignition column depth inferred from observations, $y_{\text{ign,obs}} =$

^{*} E-mail: meisel@ohio.edu

$0.5\text{--}3\times 10^{12}\text{ g cm}^{-2}$ (Cumming et al. 2006). This range for $y_{\text{ign,obs}}$ is somewhat sensitive to the neutron star envelope temperature profile that is assumed prior to the superburst (Keek et al. 2015), but this correction is not considered here.

These constraints on the superburst $y_{\text{ign,obs}}$ can be confronted with results from model calculations of carbon ignition in the accreted neutron star ocean. As is described in more detail in the following sections, ignition curves based on adopted heating and cooling rates can be paired with models of the accreted neutron star thermal structure in order to calculate y_{ign} . Comparisons of the calculated and inferred y_{ign} can place constraints on the accreted neutron star thermal structure and therefore on the magnitude and depth of shallow heating.

In this work, I perform comparisons of calculated and inferred y_{ign} in order to place constraints on the properties of the shallow heat source thought to be present in accreted neutron star crusts. In Section 2, I describe the calculations of the carbon ignition curves and crust thermal profiles, as well as the superburst ignition depth. Section 3 contains the calculation results. In Section 4, the constraints on the shallow heat source depth and magnitude are discussed, followed by a discussion of the nuclear physics uncertainties potentially impacting the results, as well as a discussion of incorporating the technique presented here into future multi-observable model-observation comparisons. Section 5 contains a summary.

2 CALCULATIONS

This work follows the y_{ign} calculation approach of Deibel et al. (2016), who closely followed the method presented by Potekhin & Chabrier (2012). For a chosen $^{12}\text{C}+^{12}\text{C}$ fusion rate and ocean thermal conductivity, the changes in the nuclear energy generation rate and in the cooling rate with a change in temperature are calculated and, at each column depth, it is determined what temperature is required for the heating derivative to exceed the cooling derivative. For an adopted set of astrophysical conditions and crust microphysics, the temperature as a function of depth is determined by numerically solving the general relativistic heat diffusion equation, in this case using the code dStar (Brown 2015). The point at which an ignition curve intersects a thermal profile is the superburst ignition depth for that set of astrophysical conditions and microphysics. Each of these steps is described in more detail in the following subsections.

2.1 Carbon Ignition Curves

Nuclear energy generation at the ignition of a superburst is set by the $^{12}\text{C}+^{12}\text{C}$ fusion rate. At temperatures relevant for the accreted neutron star envelope, this nuclear reaction rate is based on nuclear theory calculations and is uncertain by several orders of magnitude (Beck et al. 2020; Tang & Ru 2022; Aliotta et al. 2022). Modern theoretical $^{12}\text{C}+^{12}\text{C}$ rates include results from barrier penetration calculations using the Sao Paulo potential (Yakovlev et al. 2010), coupled-channel calculations performed using the M3Y+repulsion double-folding potential (Esbensen et al. 2011), empirical extrapolations based on the hindrance model (Jiang et al. 2018), experimentally derived results based on the trojan horse method (THM) (Tumino et al. 2018), THM results adopting a Coulomb renormalization (Mukhamedzhanov et al. 2019), and a microscopic model with molecular resonances (Taniguchi & Kimura 2021). Each of these are used in the present work.

Theoretical results for $^{12}\text{C}+^{12}\text{C}$ fusion are typically presented as a modified astrophysical S -factor, S^* , where the S -factor is

$S(E) = S^*(E) \exp(-0.46E)$, with E as the center-of-mass energy of the reaction. For nuclear reactions involving the fusion of two charged particles, the S -factor is related to the directly measured (or calculated) cross section $\sigma(E)$ by $\sigma(E) = S(E) \exp(-2\pi\eta)/E$, where η is defined below. Following Potekhin & Chabrier (2012), the thermonuclear fusion rate of nuclear species 1 and 2 per unit volume at temperature T in an electron-degenerate environment characterized by electron chemical potential μ_e is

$$\mathcal{R}_{12}(T, \mu_e) = \frac{w_{12}c\sqrt{8}}{\sqrt{\pi\mu_{\text{red}}m_u}(k_B T)^3} n_1(\mu_e)n_2(\mu_e)\text{INT}, \quad (1)$$

$$\text{INT} = \int_0^\infty S(E_s) \exp(-2\pi\eta(E_s) - E/(k_B T)) dE.$$

Here, c is the speed of light in vacuum, k_B is the Boltzmann constant, m_u is the nucleon mass, $w_{12} = 0.5$ for identical nuclear species and 1 otherwise, and $\mu_{\text{red}} = (A_1 A_2)/(A_1 + A_2)$ is the reduced mass of species with nuclear mass numbers A_i . The species' number densities n_i are related to μ_e via the mass-density ρ by $n_i = (X_i/A_i)\rho$, where, for an environment in which the pressure is dominated by degenerate electrons (Meisel et al. 2018),

$$\rho(\mu_e) \approx 7.2 \times 10^6 \frac{N_A}{Y_e} \left(\frac{\mu_e}{1 \text{ MeV}} \right)^3 \text{ g cm}^{-3}. \quad (2)$$

N_A is the Avogadro constant and the electron fraction $Y_e = (\sum_i Z_i X_i/A_i)/(\sum_i A_i X_i/A_i)$ is summed over all species at μ_e , where each species has nuclear charge Z_i and mass-fraction X_i .

The Sommerfeld parameter is $\eta(E) = \sqrt{(Z_1^2 Z_2^2 \alpha_{\text{fs}}^2 \mu_{\text{red}} m_u)/(2E)}$, where α_{fs} is the fine-structure constant. In order to account for the enhancement of the fusion rate due to plasma screening, both $S(E)$ and $\eta(E)$ are evaluated at a shifted energy, $E_s = E + H_{12}(0)$ (Cl rouin et al. 2019). The temperature-dependent energy shift $H_{12}(0)$ for a high-density environment can be approximated as $H_{12}(0) = k_B T h_{12}^0$, where $h_{12}^0 = f_0(\Gamma_i) + f_0(\Gamma_j) - f_0(\Gamma_{ij}^{\text{comp}})$, assuming the linear mixing rule (Chugunov & Dewitt 2009). The terms $f_0(\Gamma)$ are the Coulomb free energy per ion in a one component plasma using the analytic approximation (Potekhin & Chabrier 2000)

$$f_0(\Gamma) = a_1 \left(\sqrt{\Gamma(a_2 + \Gamma)} - a_2 \ln \left(\sqrt{\Gamma/a_2} + \sqrt{1 + \Gamma/a_2} \right) \right) \\ + 2a_3 \left(\sqrt{\Gamma} - \arctan(\sqrt{\Gamma}) \right) + b_1 (\Gamma - b_2 \ln(1 + \Gamma/b_2)) \\ + (b_3/2) \ln(1 + \Gamma^2/b_4), \quad (3)$$

where $a_1 = -0.907$, $a_2 = 0.62954$, $a_3 = 0.2771$, $b_1 = 0.00456$, $b_2 = 211.6$, $b_3 = -10^{-4}$, and $b_4 = 0.00462$. The ion coupling radii are $\Gamma_i = \alpha_{\text{fs}} \hbar c Z_i^{5/3}/(a_e k_B T)$, where \hbar is the reduced Planck constant and the electron sphere radius is $a_e = (3/(4\pi n_e(\mu_e)))^{1/3}$. The electron number density at μ_e is $n_e(\mu_e) = (Y_e/m_u)\rho(\mu_e)$. For the compound nucleus resulting from the fusion of species 1 + 2, $Z_i = Z_1 + Z_2$.

The local nuclear energy generation rate per unit mass is

$$\epsilon_{\text{nuc}} = \mathcal{R}_{12} Q_{12}/\rho, \quad (4)$$

where Q_{12} is the energy release of a fusion event between species 1 and 2.

The present work deals with $^{12}\text{C}+^{12}\text{C}$ fusion, so $w_{12} = 0.5$, $Z_1 = Z_2 = 6$, $A_1 = A_2 = 12$, Q_{12} is the absolute value of the atomic mass excess of the compound nucleus ^{24}Mg ($|\text{ME}(^{24}\text{Mg})| = 13.9336 \text{ MeV}$ (Wang et al. 2021a)), and the adopted S^* come from the aforementioned nuclear theory calculations. The envelope is as-

sumed to be comprised of only ^{12}C and ^{56}Fe , with $X_{\text{C}} = 0.2$ and $X_{\text{Fe}} = 0.8$.

The local cooling rate per unit mass from thermal diffusion is (Fujimoto et al. 1981; Potekhin & Chabrier 2012)

$$\epsilon_{\text{cool}} = \kappa_{\text{eff}} \rho T / y^2, \quad (5)$$

where $\kappa_{\text{eff}} = 0.17\kappa$ is the effective thermal conductivity. The thermal conductivity $\kappa = \pi^2 c^2 k_{\text{B}}^2 T n_e / (3\mu_e \nu_{\text{coll}})$ (Meisel et al. 2018), where the collision frequency ν_{coll} in a liquid ocean is determined by the electron-ion impurity using the linear mixing rule approximation (Brown 2004): $\nu_{\text{coll}} = 4\alpha_{\text{fs}}^2 \mu_e \langle Z^2 \Lambda_{\text{ei}} \rangle / (3\pi \hbar \langle Z \rangle)$. Here, $\langle \rangle$ are mass-fraction-weighted averages of the composition at μ_e and $\Lambda_{\text{ei}} = 1$ is the Coulomb logarithm, where it is noted that a more accurate estimate of Λ_{ei} would consider the accreted neutron star envelope structure (Horowitz & Berry 2009; Roggero & Reddy 2016). For an environment in which the pressure is dominated by degenerate electrons, the column depth y is related to μ_e by (Meisel et al. 2018)

$$y \approx 7.2 \times 10^9 \left(\frac{\mu_e}{1 \text{ MeV}} \right)^4 \frac{2.44 \times 10^{14} \text{ cm s}^{-2}}{g} \text{ g cm}^{-2}. \quad (6)$$

The local gravitational acceleration is $g = (GM_{\text{NS}}/R_{\text{NS}}^2)(1+z)$, where G is the gravitational constant, M_{NS} is the neutron star mass, and the surface gravitational redshift is $(1+z) = 1/\sqrt{1 - 2GM_{\text{NS}}/(R_{\text{NS}}c^2)}$.

Thermal instability for superburst ignition is achieved when the change in the nuclear heating rate outpaces the change in the cooling rate with a change in temperature (Fushiki & Lamb 1987):

$$\frac{\partial \epsilon_{\text{nuc}}}{\partial T} > \frac{\partial \epsilon_{\text{cool}}}{\partial T}. \quad (7)$$

The carbon ignition curves shown in Figure 1 were calculated by identifying the minimum T needed to satisfy this inequality at each y located within part of the neutron star ocean and outer crust.

2.2 Crust Thermal Profiles

Thermal profiles (i.e. temperature as a function of depth) for the accreted neutron star crust were calculated for a large number of somewhat arbitrarily chosen but astrophysically relevant conditions using the open-source code dStar (Brown 2015). In dStar, the thermal evolution of a neutron star undergoing (or having undergone) accretion is calculated by solving the general relativistic heat diffusion equation using the MESA (Paxton et al. 2011, 2013, 2015) numerical libraries with the microphysics described by Brown & Cumming (2009). The input file for a dStar calculation is known as an *inlist*, as shown in Appendix A, which can be used to specify a number of astrophysical parameters, microphysics models, and numerical controls. Key input quantities are described in this subsection. In addition, Tables 1 and 2 list the input parameters that were varied between calculations.

Accretion drives the neutron star outer layers out of thermal equilibrium with the core, where heat is deposited into the crust via nuclear reactions that are driven by accretion, which can also lead to neutrino cooling (Lau et al. 2018; Schatz et al. 2022b). The thermal profile, and thereby the temperature at each radial coordinate r (assuming spherical symmetry), over time t is determined via the heat diffusion equation (Page & Reddy 2013):

$$C_V \frac{\partial T}{\partial t} = \kappa \frac{\partial^2 T}{\partial r^2} + \frac{1}{r^2} \frac{\partial (r^2 \kappa)}{\partial r} \frac{\partial T}{\partial r} + Q_{\text{heat}} - Q_{\text{cool}}, \quad (8)$$

where the specific heat C_V (described in detail by Brown & Cumming

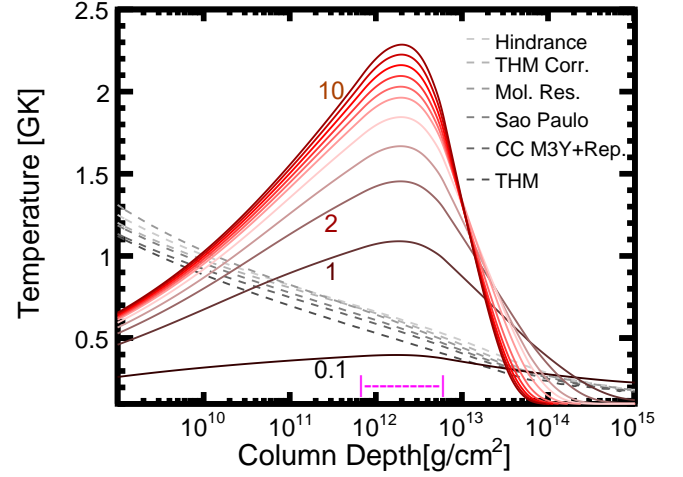


Figure 1. Carbon ignition curves (gray dashed-lines) for $^{12}\text{C}+^{12}\text{C}$ fusion rates used in this work: Hindrance (Jiang et al. 2018), THM Corr. (Mukhamedzhanov et al. 2019), Mol. Res. (Taniguchi & Kimura 2021), Sao Paulo (Yakovlev et al. 2010), CC M3Y+Rep. (Esbensen et al. 2011), and THM (Tumino et al. 2018). The order of rates in the legend is the order (from high-to-low T) of the ignition curves at $y = 10^{12} \text{ g cm}^{-2}$. Thermal profiles (red solid lines) calculated with dStar for the maximum urca cooling scenario are also shown, where $\dot{M} = 1.75 \times 10^{-8} M_{\odot} \text{ yr}^{-1}$, $Q_{\text{imp}} = 4$, and $\Delta t = 1643.6 \text{ d}$. Shallow heating was deposited in the range indicated by the pink |---|, with $Q_{\text{sh}} = 0.1 \text{ MeV } u^{-1}$ and $1 - 10 \text{ MeV } u^{-1}$ in steps of 1 MeV , as indicated by the labels next to the profiles.

(2009)), κ , nuclear heating rate Q_{heat} , and neutrino cooling rate Q_{cool} are each depth dependent. The neutron star core can be approximated as an infinite heat sink, though this is not quite the case (Cumming et al. 2017; Brown et al. 2018), fixing the temperature at the crust-core boundary to the core temperature T_{core} . In this work, $T_{\text{core}} = 10^8 \text{ K}$ based on typical constraints for several crust-cooling systems (Page & Reddy 2013; Degenaar et al. 2014; Deibel et al. 2015; Lalit et al. 2019).

In the crust, κ is related to the variance in the nuclear charge of the composition, as described in Section 2.1; however, the composition is generally not the same as in the ocean. It is customary to describe the charge variance in the accreted neutron star crust by the impurity parameter (Itoh & Kohyama 1993; Brown & Cumming 2009):

$$Q_{\text{imp}} = \frac{\sum_i n_i (Z_i - \langle Z \rangle)^2}{\sum_i n_i}. \quad (9)$$

In reality, Q_{imp} evolves over depth due to nuclear reactions and due to changing surface burning over time, e.g. because of changing \dot{M} . However, both the nuclear physics of crust reactions and the surface burning history of a given accreting neutron star system have significant uncertainties. It is therefore more common to employ a single approximate Q_{imp} in model-observation comparisons. In this work, $Q_{\text{imp}} = 4$ and 40 are adopted, where the former has successfully explained crust-cooling observations of the superbursting system KS 1731-26 (Lalit et al. 2019) and the latter is the largest Q_{imp} yet used to reproduce any observed crust-cooling light curve (Degenaar et al. 2014).

Here, deep crustal heating is approximated by depositing 1.5 MeV per accreted nucleon ($\text{MeV } u^{-1}$) across $y = 5 \times 10^{15} - 2 \times 10^{17} \text{ g cm}^{-2}$ and e^- -capture heating is approximated by depositing $0.3 \text{ MeV } u^{-1}$ across $y = 5 \times 10^{12} - 2 \times 10^{15} \text{ g cm}^{-2}$, consistent with recent estimates (Gupta et al. 2008; Haensel & Zdunik 2008). Absent a physical

model, shallow heating of strength Q_{sh} is deposited uniformly about a column depth y_{sh} within the range $y_{\text{sh}}/3$ to $3y_{\text{sh}}$, following [Deibel et al. \(2015\)](#). Each of the shallow heating magnitudes and depths listed in [Table 1](#) was employed in combination with each of the other input parameter options. The range of Q_{sh} adopted was 0.1 – $10 \text{ MeV } u^{-1}$ in steps of 0.1 , where the lower-bound is equivalent to using a higher-end estimate for e^- -capture heating and the upper estimate is the maximum Q_{sh} thus far inferred from accreting neutron star model-observation comparisons ([Deibel et al. 2015](#)). Rather than selecting the shallow heating depth in terms of y_{sh} , this depth was selected on a grid of pressure P_{sh} over the range $\log(P_{\text{sh}}) = 24$ – 29 , in cm-g-s units, in steps of 0.05 . This is intended to encompass the range of y_{sh} found to be plausible by crust cooling model-observation comparisons ([Deibel et al. 2015](#); [Merritt et al. 2016](#); [Parikh et al. 2018](#); [Ootes et al. 2019](#); [Page et al. 2022](#)). For this depth range, where the pressure is primarily due to electron degeneracy, the pressure $P = \mu_e^4 / (12\pi^2 \hbar^3 c^3)$ ([Meisel et al. 2018](#)).

The total amount of heat deposited into the accreted neutron star outer layers during an accretion outburst depends on the duration Δt and average \dot{M} of the accretion outburst. The two values for \dot{M} used in this work are approximately 10% and 100%, respectively, of the Eddington accretion rate for a standard neutron star accreting hydrogen-rich fuel ([Schatz et al. 1999](#)). The smaller accretion rate is in the range typically inferred for superbursting systems ([in't Zand 2017](#)) and the larger is roughly the accretion rate at which stable burning begins ([Galloway & Keek 2021](#)). Here, dStar thermal profiles were recorded for each calculation at Δt of 1643.6 d and 4565 d. The former is the Δt required to replace the envelope down to $y = 10^{12} \text{ g cm}^{-2}$ at 10% Eddington accretion rate, while the latter is the duration of the accretion outburst observed for KS 1731-26 prior to going into quiescence in 2001 ([Merritt et al. 2016](#)). Neither of these Δt are sufficient to reach a steady-state temperature profile, but the longer of the two is close to achieving that state ([Page & Reddy 2013](#)).

Neutrinos can be emitted from spherical shells in the crust via e^- -capture/ β^- -decay cycling, known as urca cooling ([Schatz et al. 2014](#)). The neutrino luminosity L_ν associated with e^- -capture parent species (Z_i, A_i) with mass fraction X_i is ([Tsuruta & Cameron 1970](#); [Deibel et al. 2016](#)):

$$L_{\nu,i} \approx L_{34} \times 10^{34} \text{ erg s}^{-1} X_i T_9^5 \left(\frac{g_{14}}{2}\right)^{-1} R_{10}^2, \quad (10)$$

where T_9 is the temperature of the urca shell in units of 10^9 K , $R_{10} \equiv R_i / (10 \text{ km})$, $R_i \approx R_{\text{NS}}$ is the radius of the urca shell from the neutron star center, and $g_{14} \equiv g / (10^{14} \text{ cm s}^{-2})$. $L_{34}(Z_i, A_i)$ is the intrinsic cooling strength:

$$L_{34} = 0.87 \left(\frac{10^6 \text{ s}}{ft}\right) \left(\frac{56}{A_i}\right) \left(\frac{|Q_{\text{EC}}|}{4 \text{ MeV}}\right)^5 \left(\frac{\langle F \rangle^*}{0.5}\right). \quad (11)$$

The energy-cost for e^- -capture is the e^- -capture Q -value $Q_{\text{EC}} = \text{ME}(Z_i, A_i) - \text{ME}(Z_i - 1, A_i)$, where the atomic mass excesses ME are corrected by a Coulomb lattice energy $+C_\ell Z^{5/3} Q_{\text{EC},0}$, $Q_{\text{EC},0}$ is the Q -value without the lattice correction, and $C_\ell \approx 3.407 \times 10^{-3}$ ([Roca-Maza & Piekarewicz 2008](#)). The factor $\langle F \rangle^* \equiv \langle F \rangle^+ \langle F \rangle^- / (\langle F \rangle^+ + \langle F \rangle^-)$, where the Coulomb factor $\langle F \rangle^\pm \approx 2\pi\alpha_{\text{fs}} Z_i / |1 - \exp(\mp 2\pi\alpha_{\text{fs}} Z_i)|$. The comparative half-life of the weak transition ft is the average for the β^- -decay and e^- -capture reactions in the urca cycle, $ft = (ft_\beta + ft_{\text{EC}})/2$, where the two are related by the spin J degeneracy of the initial states $ft_\beta / (2J_\beta + 1) = ft_{\text{EC}} / (2J_{\text{EC}} + 1)$ [Paxton et al. \(2016\)](#). In principle, Equation 11 can be modified by the thermal population of nuclear excited states ([Wang et al. 2021b](#)), but they are ignored in the present work.

Table 1. dStar input parameters which were varied for the large grid of calculations performed in this work, where ‘‘cgs’’ indicates in cm-g-s units. Note that \dot{M} and Q_{imp} each only had two settings. Urca cooling settings are described in [Table 2](#).

Parameter	Lower Bound	Upper Bound	Step Size
\dot{M} [$M_\odot \text{ yr}^{-1}$]	1.75×10^{-9}	1.75×10^{-8}	-
Q_{sh} [$\text{MeV } u^{-1}$]	0.1	10	0.1
$\log(P_{\text{sh}} [\text{cgs}])$	24	29	0.05
Q_{imp}	4	40	-

Table 2. Urca cooling conditions used in dStar calculations for this work, where ‘‘cgs’’ indicates in cm-g-s units. All other varied inputs are described in [Table 1](#).

Mode	$X(A)L_{34}$	$\log(P_{\text{urca}} [\text{cgs}])$
None	0	-
Minimum	4.47×10^{-2}	29.135
Nominal	4.80	29.159
Maximum	5.15×10^2	29.184

For simplicity, the present work is limited to investigating the impact of urca cooling from ^{55}Sc – ^{55}Ca , as this pair is thought to have more than an order of magnitude larger L_ν than the next most significant urca pair ([Deibel et al. 2016](#); [Meisel & Deibel 2017](#)) when adopting superburst ashes, where $X(A = 55) = 0.018$ ([Schatz et al. 2014](#); [Keek et al. 2012](#)). Four sets of urca cooling conditions were investigated, summarized in [Table 2](#). For the no-cooling scenario, corresponding to an absence of ^{55}Sc at the appropriate depth ($\mu_e \approx Q_{\text{EC}}$), $XL_{34} = 0$. The nominal cooling scenario corresponds to using the current best estimates for $Q_{\text{EC},0}$ and ft , while the maximum and minimum cooling scenarios correspond to upper and lower limits calculated based on the uncertainties for these parameters. For consistency, the pressure at which the urca shell is located P_{urca} is modified corresponding to $Q_{\text{EC},0}$. In this work, $|Q_{\text{EC},0}| = 12.192 \text{ MeV}$ is calculated using ME from [Michimasa et al. \(2018\)](#); [Leistenschneider et al. \(2021\)](#) and the associated uncertainty $\delta Q_{\text{EC},0} = 0.172 \text{ MeV}$ is calculated using their one-standard-deviation uncertainties. I use $ft = 5.9$ and associated uncertainty $\delta ft = 2$ based on the systematics of [Singh et al. \(1998\)](#), as experimental constraints do not yet exist for this weak transition.

To summarize the presentation of the thermal profile calculations, 161 600 dStar calculations were performed, using all combinations of the input parameters and urca cooling conditions detailed in [Tables 1](#) and [2](#), respectively. Example thermal profiles are shown in [Figure 1](#).

2.3 Superburst Ignition Depth

For a single carbon ignition curve and thermal profile, y_{ign} is determined by numerically finding the intersection of the two. In a physical system, carbon will accumulate until a sufficient depth is reached for ignition, and as such the shallowest- y intersection is the one of interest. The y_{ign} was determined for each combination of the six carbon ignition curves described in [Section 2.1](#) and the 161 600 thermal profiles described in [Section 2.2](#).

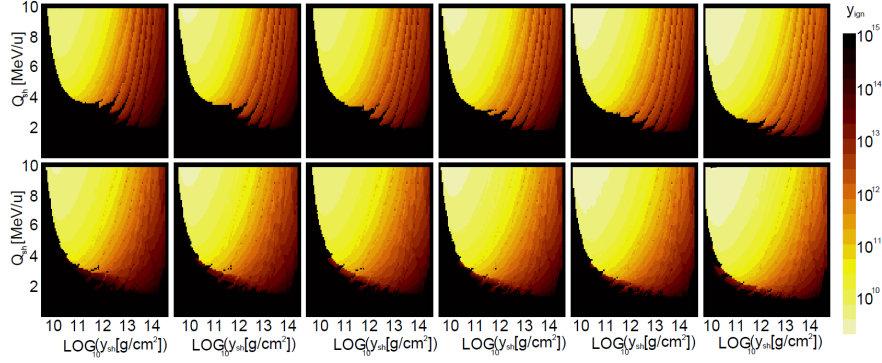
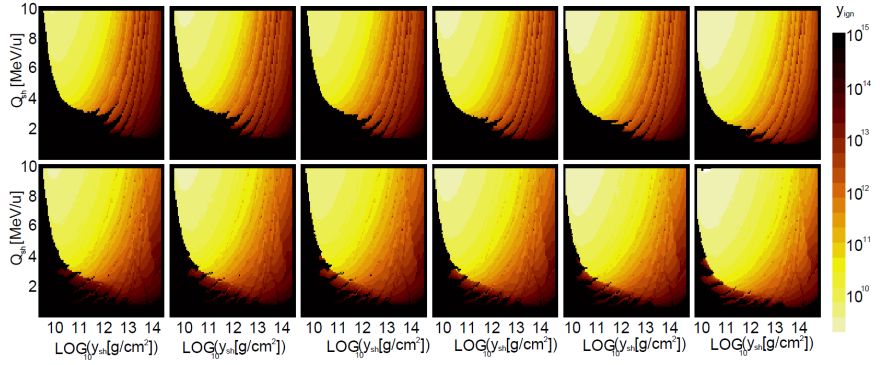
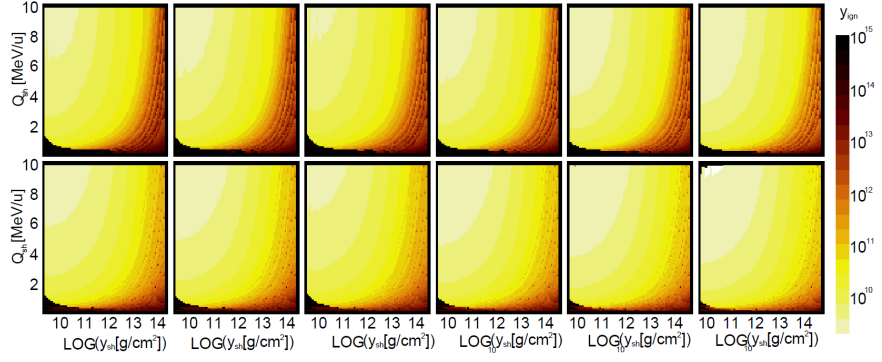
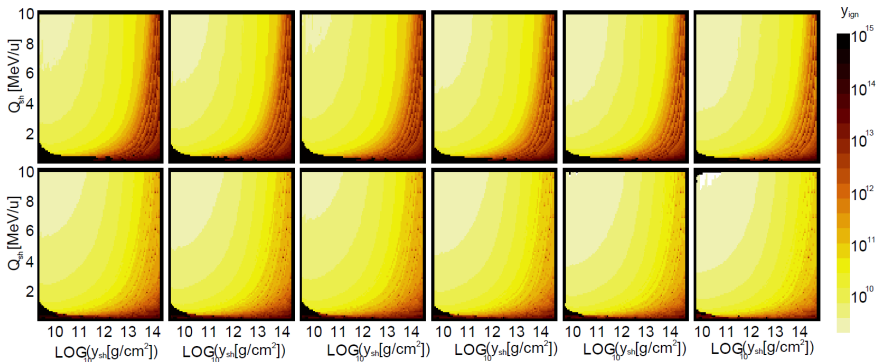

 (a) $Q_{\text{imp}} = 4$, $\dot{M} = 1.75 \times 10^{-9} M_{\odot} \text{ yr}^{-1}$, Urca=None

 (b) $Q_{\text{imp}} = 40$, $\dot{M} = 1.75 \times 10^{-9} M_{\odot} \text{ yr}^{-1}$, Urca=None

 (c) $Q_{\text{imp}} = 4$, $\dot{M} = 1.75 \times 10^{-8} M_{\odot} \text{ yr}^{-1}$, Urca=None

 (d) $Q_{\text{imp}} = 40$, $\dot{M} = 1.75 \times 10^{-8} M_{\odot} \text{ yr}^{-1}$, Urca=None

Figure 2. Calculated y_{ign} in units of g cm^{-2} (indicated by color, where black indicates that the conditions for y_{ign} were not satisfied) for the modeled range of y_{sh} and Q_{sh} using the indicated Q_{imp} and \dot{M} , without an urca cooling layer. Columns of figures correspond to a particular $^{12}\text{C}+^{12}\text{C}$ reaction rate, from left to right and using the labels of Figure 1: Hindrance, THM Corr., Mol. Res., Sao Paulo, CC M3Y+Rep., THM. In each subfigure, the upper row corresponds to $\Delta t = 1643.6$ d, while the lower row corresponds to $\Delta t = 4565$ d.

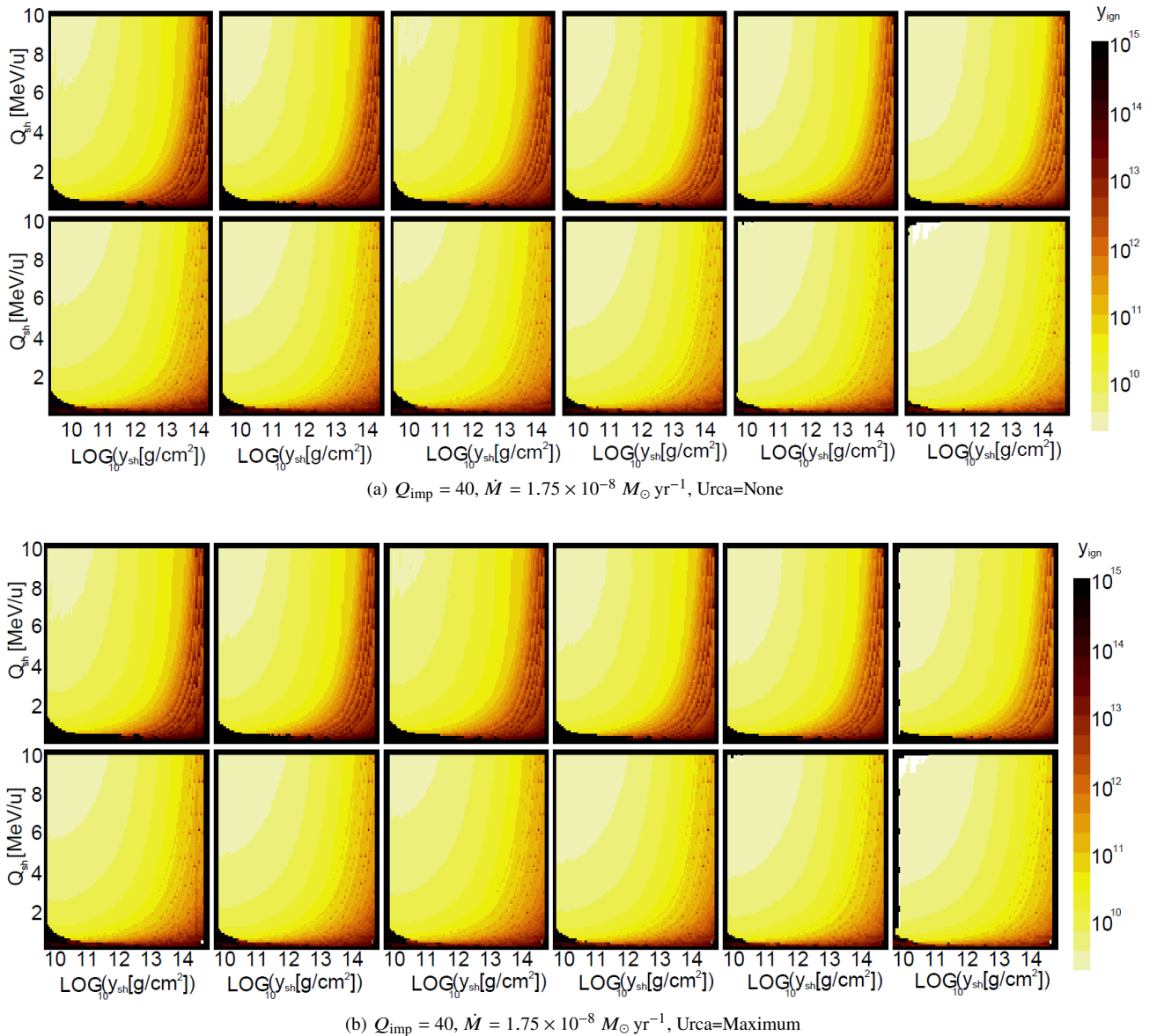


Figure 3. Same as Figure 2, highlighting the Q_{imp} , \dot{M} case where urca cooling has the most significant impact on the y_{ign} landscape.

3 RESULTS

Figure 2 shows y_{ign} resulting from Section 2.3 for calculations performed with the no urca cooling scenario. The columns of the subfigures show the impact of adopting different $^{12}\text{C}+^{12}\text{C}$ reaction rates, while the rows of the subfigures show the impact of Δt . The solid-black regions in these figures correspond to cases where the conditions for y_{ign} were not met, i.e. the carbon ignition curve and thermal profile did not intersect within $y = 10^{10} - 10^{15} \text{ g cm}^{-2}$. For all cases, y_{ign} is relatively shallow for large Q_{sh} and shallow y_{sh} , while y_{ign} is relatively deep for the opposite scenario. Contours of approximately equal y_{ign} follow a trajectory of increasing Q_{sh} and deepening y_{sh} . However, the contours abruptly end for low Q_{sh} and shallow y_{sh} . This is because insufficient heat is deposited and retained within the neutron star outer layers in order for the thermal profile to intersect the ignition curve. For low \dot{M} , this region spans a considerable portion of the phase-space, even failing to achieve carbon ignition for $Q_{\text{sh}} \approx 9 \text{ MeV u}^{-1}$ if $y_{\text{sh}} \approx 10^{10} \text{ g cm}^{-2}$.

The gradient of y_{ign} within the $Q_{\text{sh}}-y_{\text{sh}}$ phase space becomes steeper moving from large Q_{sh} and shallow y_{sh} to small Q_{sh} and deep y_{sh} . This can be understood by considering Figure 1. The thermal profile for small Q_{sh} has a relatively shallow slope $\partial T/\partial y$, while $\partial T/\partial y$ rapidly increases in magnitude for increasing Q_{sh} , approaching a converged slope. For deep y_{sh} , the thermal profile intersects the carbon ignition curve at deep y , where the carbon ignition curve slope is especially shallow. As such, for small Q_{sh} and deep y_{sh} , y_{ign} depends on the intersection of two shallow-sloped curves, which will be particularly sensitive to small changes in the slope of the thermal profile, leading to a more rapid change in y_{ign} in this region of the $Q_{\text{sh}}-y_{\text{sh}}$ phase-space.

The results shown in Figure 2 demonstrate a weak sensitivity to Q_{imp} and $^{12}\text{C}+^{12}\text{C}$ rate, as well as a modest sensitivity to Δt . Of all parameters investigated in this work, y_{ign} is primarily sensitive to \dot{M} . While both \dot{M} and Δt impact Q_{heat} deposited within the crust, Δt controls how close the thermal profile is to steady-state, while

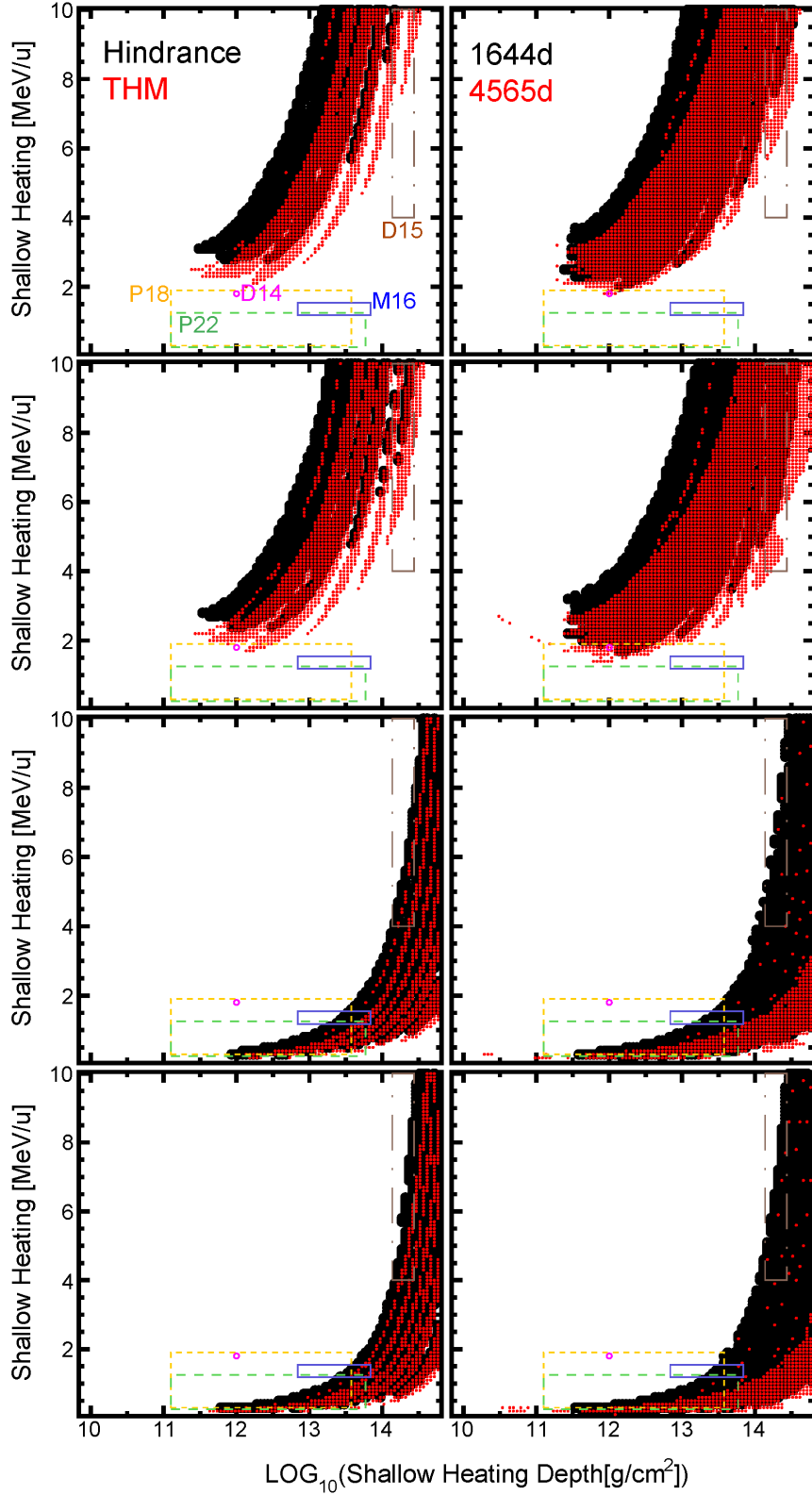


Figure 4. Map of regions in which the calculated y_{ign} is within the inferred range $y_{\text{ign,obs}} = 0.5 - 3 \times 10^{12} \text{ g cm}^{-2}$, where rows correspond to the same model conditions as the rows of Figure 2. In the left column, the solid-black and dotted-red regions correspond to using the Hindrance and THM $^{12}\text{C}+^{12}\text{C}$ rates, respectively, with $\Delta t = 1643.6 \text{ d}$. In the right column, solid-black and dotted-red regions correspond to $\Delta t = 1643.6 \text{ d}$ and 4565 d , respectively, where results for all $^{12}\text{C}+^{12}\text{C}$ rates are shown. Constraints on Q_{sh} and y_{sh} obtained from fits to crust cooling sources are shown for comparison, where EXO 0748-676 (D14 (Degenaar et al. 2014)) is the pink open circle, MXB 1659-29 (P18 (Parikh et al. 2018)) is the yellow short-dashed box, KS 1731-26 (M16 (Merritt et al. 2016)) is the blue solid box, and MAXI J0556-332 (D15 (Deibel et al. 2015), P22 (Page et al. 2022)) constraints are the brown dot-dash and green long-dashed boxes, respectively.

\dot{M} decides what the steady-state thermal profile is. Here, both Δt were sufficiently close to achieving steady-state that the difference in thermal profiles is relatively modest. This would not necessarily be the case for an abnormally short Δt , as observed for 4U 1608-522 (Keek et al. 2008). Similarly, Q_{imp} impacts κ and therefore the thermal diffusion time, but does not have a particularly strong impact on the steady-state thermal profile.

Results were very nearly identical when including urca cooling. The only scenario in which urca cooling was observed to have some impact was $Q_{\text{imp}} = 40 \dot{M} = 1.75 \times 10^{-8} M_{\odot} \text{ yr}^{-1}$. This (extremely modest) impact is shown in Figure 3, where implementing the maximum urca cooling scenario slightly changes y_{ign} at low Q_{sh} and deep y_{sh} . Upon close inspection, one sees urca cooling drives y_{ign} slightly deeper around $Q_{\text{sh}} \approx 2 \text{ MeV } u^{-1}$, $\log(y_{\text{sh}} [\text{g cm}^{-2}]) \approx 14.5$ for $\Delta t = 4565 \text{ d}$. Consulting Figure 1, it is apparent that the impact of shallow heating on the thermal profile is mostly concentrated near y_{sh} . Given the strong T -dependence of L_{ν} (see Equation 10), urca cooling will result in an insignificant Q_{cool} unless y_{sh} approaches y_{urca} , consistent with the findings of Deibel et al. (2016). Note that the present work only considers the impact of the ^{55}Sc – ^{55}Ca urca pair, which is located in the crust. The impact of urca cooling may be more significant when considering an urca pair located in the accreted neutron star ocean, though there the strong Q_{EC} -dependence will reduce L_{ν} (see Equation 11) and therefore Q_{cool} .

Figure 4 shows the regions from Figure 2 where y_{ign} calculated in this work is within the ignition depth inferred from model-observation comparisons of superburst light-curves, $y_{\text{ign,obs}} = 0.5 - 3 \times 10^{12} \text{ g cm}^{-2}$ (Cumming et al. 2006). The left and right columns of this figure show the influence of the $^{12}\text{C}+^{12}\text{C}$ reaction rate and Δt , respectively. For comparison, Figure 4 includes constraints on shallow heating obtained from fits to crust cooling light curves performed in earlier works. These include the results of fits to EXO 0748-676 (Degenaar et al. 2014), MXB 1659-29 (Parikh et al. 2018), KS 1731-26 (Merritt et al. 2016), and MAXI J0556-332 (Deibel et al. 2015; Page et al. 2022), of which it is noted that only KS 1731-26 has been observed to feature superbursts. The two constraints for MAXI J0556-332 are quite disparate, as Page et al. (2022) assumed that the first crust cooling event observed for this source was shortly preceded by a hyperburst within the crust, while Deibel et al. (2015) fit only this cooling event while assuming shallow heating was responsible for the large energy deposition in the neutron star outer layers. For the low \dot{M} modeled in this work, which is closer to the \dot{M} observed prior to superbursts (in't Zand 2017), the shallow heating constraints obtained in the present work are on the edge of consistency with crust cooling constraints. Here, for the lower of the two \dot{M} , the present work favors generally larger Q_{sh} and deeper y_{sh} , with the exception of the unique findings of Deibel et al. (2015). For \dot{M} near the Eddington limit, the present work results in shallow heating that is in agreement with most constraints from crust cooling model-observation comparisons, but skewing to deeper y_{sh} . For large \dot{M} , there is stronger sensitivity of y_{ign} to Δt at deep y_{sh} .

4 DISCUSSION

4.1 Shallow Heating Constraints

Figure 4 demonstrates that the inferred depth of carbon ignition for superbursts can be used as a constraint for the magnitude and depth of shallow heating in accreting neutron stars. This constraint is primarily sensitive to \dot{M} , modestly sensitive to Δt and the $^{12}\text{C}+^{12}\text{C}$ reaction rate, weakly dependent on Q_{imp} , and negligibly dependent

on urca cooling in the accreted crust. The primary sensitivity, \dot{M} , can usually be constrained for a superbursting system based on the persistent luminosity (though there are complications related to X-ray reflection from the accretion disk) (He & Keek 2016). Therefore, this shallow heating constraint is relatively robust to changes in modeling assumptions.

Relative to the complementary constraints on shallow heating from crust cooling model-observation comparisons, the superburst ignition depth constraint is weaker in that it allows for a larger region of the Q_{sh} – y_{sh} phase-space. This is to be expected, as y_{ign} essentially only depends on the thermal structure at a single y , while crust cooling light curves depend on the thermal structure of the entire neutron star. However, the superburst ignition depth constraint offers the distinct advantage of being insensitive to Q_{imp} and urca cooling, contrary to crust cooling light curves (Brown & Cumming 2009; Meisel & Deibel 2017). Furthermore, most superbursting sources do not feature crust cooling episodes (Galloway et al. 2020) and therefore the method presented here can expand the set of accreting neutron stars that can be used to constrain shallow heating.

Of the crust-cooling sources featured in Figure 4, only KS 1731-26 has also exhibited a superburst. The \dot{M} inferred from the persistent X-ray luminosity prior to the superburst event is $\approx 10\%$ of Eddington (Kuulkers et al. 2002), corresponding to the lower \dot{M} modeled in the present work. This \dot{M} is in agreement with the \dot{M} that one would infer based on the recurrence time between KS1731-26 X-ray bursts prior to the superburst (Lampe et al. 2016; Meisel et al. 2019). Fits to the KS 1731-26 crust-cooling light curve infer that $Q_{\text{imp}} \approx 4$ (Merritt et al. 2016; Lalit et al. 2019). The Δt prior to the quiescent episode of KS 1731-26 in 2001 is assumed to be 4565 d based on observational data (Merritt et al. 2016), implying that Δt prior to the 1998 superburst event was $\Delta t \approx 2900 \text{ d}$. Therefore, the results from the present work that are most relevant for KS 1731-26 are from the calculations with $Q_{\text{imp}} = 4$ and $\dot{M} = 1.75 \times 10^{-9} M_{\odot} \text{ yr}^{-1}$. These results do not appear to be consistent with the shallow-heating constraints obtained by crust-cooling light curve fits in Merritt et al. (2016) (blue solid box in Figure 4). However, given the approximate nature of the \dot{M} constraints prior to the superbursting episode, it is plausible that consistency could be achieved. More detailed analysis, e.g. of the persistent X-ray luminosity prior to the superburst or model-observation comparisons for the light curve shape and recurrence time of standard bursts (Meisel 2018; Johnston et al. 2020), is likely necessary. Additionally, while the crust-cooling models of Merritt et al. (2016) fit for Q_{sh} , they held y_{sh} fixed. It is therefore possible that the inconsistency between their Q_{sh} constraints and this work are due to fixing y_{sh} in that work. Further crust-cooling model-observation comparisons are needed to draw stronger conclusions.

4.2 Influence of Nuclear Physics Uncertainties

The shallow heating constraints obtained in this work are relatively insensitive to assumptions regarding input nuclear physics. This includes not only the $^{12}\text{C}+^{12}\text{C}$ nuclear reaction rate, but also past surface burning and nuclear reactions occurring within the accreted crust.

As shown in Figures 1 and 2, adopting different $^{12}\text{C}+^{12}\text{C}$ reaction rates leads to minor changes in the calculated y_{ign} . When comparing the two most discrepant theoretical predictions for this rate, which differ in S^* by nearly six orders of magnitude (Tang & Ru 2022), the change in y_{ign} is roughly a factor of four. This relative insensitivity is due to the extreme temperature dependence of the $^{12}\text{C}+^{12}\text{C}$ rate, owing to the considerable Coulomb barrier. Nonetheless, the impact

is on the same order of the uncertainty in the inferred $y_{\text{ign,obs}}$ and so some uncertainty reduction in the $^{12}\text{C}+^{12}\text{C}$ rate would be beneficial. It would be particularly beneficial to push direct measurements of this nuclear reaction cross section down to slightly lower energies in order to confirm or exclude the THM (Tumino et al. 2018) and Hindrance (Jiang et al. 2018) rates, which are responsible for the bulk of the impact found in the present work. Based on the relative S^* of theoretical models, it appears that direct measurements of $^{12}\text{C}+^{12}\text{C}$ down to $E = 2.25$ MeV may suffice. Though Tan et al. (2020) reach $E = 2.20$ MeV for their lowest-energy measurement, that data-point is a relatively large upper-limit on S^* and has a large E -separation from the neighboring points measured in that work, making it difficult to confront with theoretical predictions.

For all accreting neutron star systems, the crust composition is uncertain due to uncertainties in which surface-burning modes (i.e. stable burning, superbursts, or X-ray bursts) were prevalent in the past, the nuclear physics of the surface-burning processes, and nuclear physics of the accreted crust. For instance, superburst ashes and X-ray burst ashes imply a substantially different Q_{imp} (Meisel et al. 2018). Meanwhile, individual nuclear reaction rates, and even individual nuclear masses, can have important impacts on Q_{imp} and X_i of urca nuclides (Cyburt et al. 2016; Schatz & Ong 2017; Ong et al. 2018; Meisel et al. 2019; Hoff et al. 2020; Meisel et al. 2022). Nuclear reactions in the crust further modify the crust composition, but these modifications depend sensitively on input nuclear physics, such as nuclear masses and the presence of exotic reaction processes (Shchechilin & Chugunov 2019; Schatz et al. 2022b). Furthermore, even if X_i were known, the L_ν themselves are sensitive to the adopted Q_{EC} and ft , which are often not known (Meisel et al. 2015; Ong et al. 2020). The insensitivity of results in the present work regarding the adopted Q_{imp} and urca cooling imply that these considerable uncertainties in the crust composition and L_ν are mostly inconsequential. The caveat to this statement is that the present work only considered an urca pair in the crust, which may not apply to an urca pair located closer to y_{sh} in the ocean. Furthermore, it is important to highlight that the surface-burning production of ^{12}C is extremely important, as it sets X_{C} in the ignition curve calculations. The mechanism to produce sufficiently high X_{C} is uncertain, but appears to require the system to spend some time in a special region of \dot{M} (Stevens et al. 2014; Keek & Heger 2016).

The remaining nuclear physics uncertainties that were not investigated in this work include e^- -capture heating and deep crustal heating, where the latter is primarily dependent on the crust-core transition pressure and hence the dense-matter equation-of-state (Shchechilin et al. 2021, 2022). Neither of these heat sources would remove the need for shallow heating, but they do impact the accreting neutron star thermal profile and therefore likely have some influence on the shallow heating constraints inferred from y_{ign} (Cooper et al. 2009).

Other important microphysics uncertainties that were not investigated in the present work include the Coulomb logarithm and plasma-screening for carbon ignition. Neither are accessible in terrestrial laboratory experiments in the foreseeable future (with the exception of plasma-screening effects for nuclear reactions of light nuclides at modest densities (Kemp et al. 2019)) and therefore dedicated theoretical efforts will be required. Once the physical origin of shallow heating is eventually determined, it is possible that y_{ign} model-observation comparisons like the ones presented here can provide some constraints.

4.3 Incorporation into Multi-observable Modeling

The method for obtaining shallow heating constraints presented in this work could be applied to any accreting neutron star system featuring superbursts. However, the value of these constraints would be increased by combining them with constraints derived from other observables. The source KS 1731-26 is particularly promising in this regard, as it features X-ray bursts that resemble the successfully modeled (Meisel et al. 2018; Johnston et al. 2020) bursts of GS 1826-24 (Muno et al. 2000), photospheric radius expansion bursts that can be used to get M_{NS} and R_{NS} constraints (Özel et al. 2012), superbursts (Kuulkers et al. 2002), and an episode of crust cooling (Rutledge et al. 2002).

Ideally, multi-observable modeling of a source such as KS 1731-26 would use consistent assumptions for the system properties across the models. However, as shown in this work, the exact crust composition need not be used for shallow heating constraints from calculations of y_{ign} . Ignoring this complication would reduce the computational cost of incorporating the y_{ign} shallow heating constraints into the multi-observable modeling.

5 CONCLUSIONS

The present work demonstrates that the inferred depth of carbon ignition for X-ray superbursts can be used to constrain the depth and magnitude of shallow heating in the accreted neutron star crust. This constraint is shown to be weakly sensitive to input nuclear physics, including assumptions regarding the $^{12}\text{C}+^{12}\text{C}$ nuclear reaction rate and the crust composition. The main model sensitivity is the accretion rate \dot{M} prior to the superburst, along with the accretion outburst duration Δt , if Δt is comparable to thermal time at the depth of the shallow heat source. This method provides a new way to constrain shallow heating, expanding the number of accreting neutron star sources that can be used for this purpose. For sources featuring other observables such as crust cooling, the inclusion of this method into multi-observable modeling may improve the stringency of constraints on shallow heating.

ACKNOWLEDGEMENTS

I thank Hendrik Schatz, Wei Jia Ong, and Duncan Galloway for useful discussions, Xiadong Tang for providing tables of the $^{12}\text{C}+^{12}\text{C}$ S^* -factors, Ed Brown for creating and maintaining a public release of dStar, and the MESA developers for creating and maintaining a public release of that code and the associated software development kit. This work was supported by the U.S. Department of Energy Office of Science under Grants No. DE-FG02-88ER40387 and DE-SC0019042 and the U.S. National Nuclear Security Administration through Grant No. DE-NA0003909. This work was inspired by conversations at a workshop that was supported by funds from the U.S. National Science Foundation under Grants No. PHY-1430152 (Joint Institute for Nuclear Astrophysics – Center for the Evolution of the Elements) and OISE-1927130 (International Research Network for Nuclear Astrophysics).

DATA AVAILABILITY

The Appendix contains a sample dStar inlist that could be used to recreate the thermal profiles used in this work. The carbon ignition curves are available as Supplementary Material.

REFERENCES

- Aliotta M., et al., 2022, *Journal of Physics G Nuclear Physics*, 49, 010501
- Beck C., Mukhamedzhanov A. M., Tang X., 2020, *European Physical Journal A*, 56, 87
- Brown E. F., 2004, *ApJ*, 614, L57
- Brown E. F., 2015, dStar: Neutron star thermal evolution code, Astrophysics Source Code Library, record ascl:1505.034 (ascl:1505.034)
- Brown E. F., Cumming A., 2009, *ApJ*, 698, 1020
- Brown E. F., Cumming A., Fattoyev F. J., Horowitz C. J., Page D., Reddy S., 2018, *Phys. Rev. Lett.*, 120, 182701
- Chamel N., Fantina A. F., Zdunik J. L., Haensel P., 2020, *Phys. Rev. C*, 102, 015804
- Chugunov A. I., Dewitt H. E., 2009, *Phys. Rev. C*, 80, 014611
- Cl rouin J., Arnault P., Desbiens N., White A. J., Collins L. A., Kress J. D., Ticknor C., 2019, *Physics of Plasmas*, 26, 012702
- Cooper R. L., Steiner A. W., Brown E. F., 2009, *ApJ*, 702, 660
- Cornelisse R., et al., 2003, *Astron. & Astrophys.*, 405, 1033
- Cumming A., Bildsten L., 2001, *Astrophys. J. Lett.*, 559, L127
- Cumming A., Macbeth J., in 't Zand J. J. M., Page D., 2006, *Astrophys. J.*, 646, 429
- Cumming A., Brown E. F., Fattoyev F. J., Horowitz C. J., Page D., Reddy S., 2017, *Phys. Rev. C*, 95, 025806
- Cyburtt R. H., Amthor A. M., Heger A., Johnson E., Keek L., Meisel Z., Schatz H., Smith K., 2016, *ApJ*, 830, 55
- Degenaar N., et al., 2014, *ApJ*, 791, 47
- Deibel A., Cumming A., Brown E. F., Page D., 2015, *Astrophys. J. Lett.*, 809, L31
- Deibel A., Meisel Z., Schatz H., Brown E. F., Cumming A., 2016, *Astrophys. J.*, 831, 13
- Deibel A., Cumming A., Brown E. F., Reddy S., 2017, *ApJ*, 839, 95
- Esbensen H., Tang X., Jiang C. L., 2011, *Phys. Rev. C*, 84, 064613
- Fantina A. F., Zdunik J. L., Chamel N., Pearson J. M., Haensel P., Goriely S., 2018, *A&A*, 620, A105
- Fujimoto M. Y., Hanawa T., Miyaji S., 1981, *ApJ*, 247, 267
- Fukushima K., Hatsuda T., 2011, *Reports on Progress in Physics*, 74, 014001
- Fushiki I., Lamb D. Q., 1987, *ApJ*, 323, L55
- Galloway D. K., Keek L., 2021, *Astrophys. Space Sc. L.*, 461, 209
- Galloway D. K., et al., 2020, *ApJS*, 249, 32
- Goodwin A. J., Galloway D. K., Heger A., Cumming A., Johnston Z., 2019, *MNRAS*, 490, 2228
- Gupta S., Brown E. F., Schatz H., M ller P., Kratz K.-L., 2007, *ApJ*, 662, 1188
- Gupta S. S., Kawano T., M ller P., 2008, *Phys. Rev. Lett.*, 101, 231101
- Haensel P., Zdunik J. L., 2008, *A&A*, 480, 459
- He C. C., Keek L., 2016, *ApJ*, 819, 47
- Hoff D. E. M., et al., 2020, *Phys. Rev. C*, 102, 045810
- Horowitz C. J., Berry D. K., 2009, *Phys. Rev. C*, 79, 065803
- Inogamov N. A., Sunyaev R. A., 2010, *Astronomy Letters*, 36, 848
- Itoh N., Kohyama Y., 1993, *ApJ*, 404, 268
- Jiang C., Santiago-Gonzalez D., Almaraz-Calderon S., Rehm K., Back B., Auranen K., 2018, *Phys. Rev. C*, 97, 012801
- Johnston Z., Heger A., Galloway D. K., 2020, *Mon. Not. R. Astron. Soc.*, 494, 4576
- Keek L., Heger A., 2016, *MNRAS*, 456, L11
- Keek L., Heger A., 2017, *ApJ*, 842, 113
- Keek L., in't Zand J. J. M., Kuulkers E., Cumming A., Brown E. F., Suzuki M., 2008, *A&A*, 479, 177
- Keek L., Heger A., in't Zand J. J. M., 2012, *ApJ*, 752, 150
- Keek L., Cumming A., Wolf Z., Ballantyne D. R., Suleimanov V. F., Kuulkers E., Strohmayer T. E., 2015, *MNRAS*, 454, 3559
- Kemp A. J., Wilks S. C., Hartouni E. P., Grim G., 2019, *Nature Communications*, 10, 4156
- Kuulkers E., et al., 2002, *A&A*, 382, 503
- Lalit S., Meisel Z., Brown E. F., 2019, *ApJ*, 882, 91
- Lampe N., Heger A., Galloway D. K., 2016, *ApJ*, 819, 46
- Lau R., et al., 2018, *ApJ*, 859, 62
- Leistenschneider E., et al., 2021, *Phys. Rev. Lett.*, 126, 042501
- Medin Z., Cumming A., 2015, *ApJ*, 802, 29
- Meisel Z., 2018, *ApJ*, 860, 147
- Meisel Z., Deibel A., 2017, *ApJ*, 837, 73
- Meisel Z., et al., 2015, *Phys. Rev. Lett.*, 115, 162501
- Meisel Z., Deibel A., Keek L., Shternin P., Elfricit J., 2018, *J. Phys. G*, 45, 093001
- Meisel Z., Merz G., Medvid S., 2019, *ApJ*, 872, 84
- Meisel Z., et al., 2022, *Phys. Rev. C*, 105, 025804
- Merritt R. L., et al., 2016, *ApJ*, 833, 186
- Michimasa S., et al., 2018, *Phys. Rev. Lett.*, 121, 022506
- Mukhamedzhanov A. M., Pang D. Y., Kadyrov A. S., 2019, *Phys. Rev. C*, 99, 064618
- Muno M. P., Fox D. W., Morgan E. H., Bildsten L., 2000, *ApJ*, 542, 1016
- Ong W. J., et al., 2018, *Phys. Rev. C*, 98, 065803
- Ong W. J., et al., 2020, *Phys. Rev. Lett.*, 125, 262701
- Ootes L. S., et al., 2019, *MNRAS*, 487, 1447
-  zel F., Gould A., G ver T., 2012, *ApJ*, 748, 5
- Page D., Reddy S., 2013, *Phys. Rev. Lett.*, 111, 241102
- Page D., Homan J., Nava-Callejas M., Cavecchi Y., Beznogov M. V., Degenaar N., Wijnands R., Parikh A. S., 2022, *ApJ*, 933, 216
- Parikh A. S., et al., 2017, *Astrophys. J. Lett.*, 851, L28
- Parikh A. S., Wijnands R., Degenaar N., Ootes L., Page D., 2018, *MNRAS*, 476, 2230
- Paxton B., Bildsten L., Dotter A., Herwig F., Lesaffre P., Timmes F., 2011, *Astrophys. J. Suppl. Ser.*, 192, 3
- Paxton B., et al., 2013, *Astrophys. J. Suppl. Ser.*, 208, 4
- Paxton B., et al., 2015, *Astrophys. J. Suppl. Ser.*, 220, 15
- Paxton B., et al., 2016, *Astrophys. J. Suppl. Ser.*, 223, 18
- Potekhin A. Y., Chabrier G., 2000, *Phys. Rev. E*, 62, 8554
- Potekhin A. Y., Chabrier G., 2012, *A&A*, 538, A115
- Riley T. E., et al., 2021, *Astrophys. J. Lett.*, 918, L27
- Roca-Maza X., Piekarewicz J., 2008, *Phys. Rev. C*, 78, 025807
- Roggero A., Reddy S., 2016, *Phys. Rev. C*, 94, 015803
- Rutledge R. E., Bildsten L., Brown E. F., Pavlov G. G., Zavlin V. E., Ushomirsky G., 2002, *ApJ*, 580, 413
- Schatz H., Ong W.-J., 2017, *Astrophys. J.*, 844, 139
- Schatz H., Bildsten L., Cumming A., Wiescher M., 1999, *ApJ*, 524, 1014
- Schatz H., Bildsten L., Cumming A., 2003, *ApJ*, 583, L87
- Schatz H., et al., 2014, *Nature*, 505, 62
- Schatz H., et al., 2022a, arXiv e-prints, p. arXiv:2205.07996
- Schatz H., et al., 2022b, *ApJ*, 925, 205
- Shchepochin N. N., Chugunov A. I., 2019, *MNRAS*, 490, 3454
- Shchepochin N. N., Gusakov M. E., Chugunov A. I., 2021, *MNRAS*, 507, 3860
- Shchepochin N. N., Gusakov M. E., Chugunov A. I., 2022, *MNRAS*, 515, L6
- Singh B., Rodriguez J. L., Wong S. S. M., Tuli J. K., 1998, *Nuc. Data Sheets*, 84, 487
- Steiner A. W., 2012, *Phys. Rev. C*, 85, 055804
- Stevens J., Brown E. F., Cumming A., Cyburtt R., Schatz H., 2014, *ApJ*, 791, 106
- Strohmayer T. E., Brown E. F., 2002, *Astrophys. J.*, 566, 1045
- Taam R. E., Picklum R. E., 1978, *ApJ*, 224, 210
- Tan W. P., et al., 2020, *Phys. Rev. Lett.*, 124, 192702
- Tang X., Ru L., 2022, in *European Physical Journal Web of Conferences*. p. 01002, doi:10.1051/epjconf/202226001002
- Taniguchi Y., Kimura M., 2021, *Physics Letters B*, 823, 136790
- Tsuruta S., Cameron A., 1970, *Astrophys. Space Sci.*, 7, 374
- Utomo A., et al., 2018, *Nature*, 557, 687
- Turlione A., Aguilera D. N., Pons J. A., 2015, *A&A*, 577, A5
- Wang M., Huang W., Kondev F., Audi G., Naimi S., 2021a, *Chinese Phys. C*, 45, 030003
- Wang L.-J., Tan L., Li Z., Misch G. W., Sun Y., 2021b, *Phys. Rev. Lett.*, 127, 172702
- Wijnands R., Degenaar N., Page D., 2017, *J. Astrophys. Astron.*, 38, 49
- Yakovlev D. G., Beard M., Gasques L. R., Wiescher M., 2010, *Phys. Rev. C*, 82, 044609
- in't Zand J., 2017, in *Serino M., Shidatsu M., Iwakiri W., Mihara*

T., eds, 7 years of MAXI: monitoring X-ray Transients. p. 121
 (arXiv:1702.04899)
 in't Zand J. J. M., Kuulkers E., Verbunt F., Heise J., Cornelisse R., 2003,
 A&A, 411, L487

APPENDIX A: SAMPLE DSTAR INLIST

The following is an example inlist for dStar (Brown 2015) calculations of the accreted crust thermal profile performed for the present work.

```
&controls
! controls for output
write_interval_for_terminal = 10000
write_interval_for_terminal_header = 10000
write_interval_for_history = 1
write_interval_for_profile = 1
starting_number_for_profile = 1

output_directory = 'LOGS'

! controls for the solver
maximum_number_of_models = 10000
maximum_timestep = 0.0
! implies that max = tend-t
integration_tolerance = 1.0d-4
! limits on temperature: if a zone goes outside these bounds, reduce stepsize
min_lg_temperature_integration = 7.0
max_lg_temperature_integration = 9.5
! spatial resolution
target_resolution_lnP = 0.05

! macroscopic NS parameters
fix_core_temperature = .TRUE.
core_temperature = 1.e8
fix_atmosphere_temperature_when_accreting = .FALSE.
atmosphere_temperature_when_accreting = 2.4d8

! integration epochs
number_epochs = 4
! 4 epochs, time in days.
!For 1.75e-8 Msol/yr eddington, 1.103e17g/s is 10pct Edd. 1.103e18g/s is 100
pct Edd
basic_epoch_Mdots = 4*1.103e+17
!Time to accrete to y=12g/cm2 for EOS radius below at 100%Edd,10%Edd; then
KS1731 outburst time
basic_epoch_boundaries = 0.0,164.4,1643.6,4565.0

! core properties for 12.31km 1.4msol NS using APR EOS, as in Lalit+2016
core_mass = 1.376 ! Msun
core_radius = 11.227 ! km
! crust boundaries (pressure)
lgPerust_bot = 32.819 ! cgs
lgPerust_top = 22.0 ! cgs

which_neutron_1S0_gap = 'sfb03'

! atmosphere composition
lg_atm_light_element_column = 4.0

! impurities
fix_Qimp = .TRUE.
Qimp = 4

! heating
turn_on_extra_heating = .TRUE.
Q_heating_shallow = 9.9
lgP_min_heating_shallow = 28.47
lgP_max_heating_shallow = 29.43

! shell Urca cooling
turn_on_shell_Urca = .TRUE.
shell_Urca_luminosity_coeff1 = 4.8
lgP_shell_Urca1 = 29.159

/
```

This paper has been typeset from a TeX/LaTeX file prepared by the author.